Bani Asadi, Hossein; Ajdary, Rubina; Trifol Guzman, Jon; Rojas, Orlando J.; Seppälä, Jukka

Direct ink writing of aloe vera/cellulose nanofibrils bio-hydrogels

Published in:
Carbohydrate Polymers

DOI:
10.1016/j.carbpol.2021.118114

Published: 15/08/2021

Document Version
Publisher's PDF, also known as Version of record

Carbohydrate Polymers 266 (2021) 118114

Contents lists available at ScienceDirect

Carbohydrate Polymers

journal homepage: www.elsevier.com/locate/carbpol

Direct ink writing of aloe vera/cellulose nanofibrils bio-hydrogels

Hossein Baniasadi [a,1], Rubina Ajdary [b,1], Jon Trifol [a], Orlando J. Rojas [b,c], Jukka Seppälä [a,*]

[a] Polymer Technology, School of Chemical Engineering, Aalto University, Kemistintie 1, 02150 Espoo, Finland
[b] Department of Bioproducts and Biosystems, School of Chemical Engineering, Aalto University, P.O. Box 16300, FIN-00076 Aalto, Espoo, Finland
[c] Bioproducts Institute, Departments of Chemical and Biological Engineering, Chemistry and Wood Science, University of British Columbia, 2360 East Mall, Vancouver, BC Canada V6T 1Z3

ARTICLE INFO

Keywords:
Aloe vera
Cellulose nanofibrils
Hydrogel
3D printing

ABSTRACT

Direct-ink-writing (DIW) of hydrogels has become an attractive research area due to its capability to fabricate intricate, complex, and highly customizable structures at ambient conditions for various applications, including biomedical purposes. In the current study, cellulose nanofibrils reinforced aloe vera bio-hydrogels were utilized to develop 3D geometries through the DIW technique. The hydrogels revealed excellent viscoelastic properties enabled extruding thin filaments through a nozzle with a diameter of 630 μm. Accordingly, the lattice structures were printed precisely with a suitable resolution. The 3D-printed structures demonstrated significant wet stability due to the high aspect ratio of the nano- and microfibrils cellulose, reinforced the hydrogels, and protected the shape from extensive shrinkage upon drying. Furthermore, all printed samples had a porosity higher than 80% and a high-water uptake capacity of up to 46 g/g. Altogether, these fully bio-based, porous, and wet stable 3D structures might have an opportunity in biomedical fields.

1. Introduction

Hydrogels are polymeric 3D structures that can preserve and release large amounts of water or biological fluids (up to thousands of times their dry weight). This class of materials with tunable mechanical properties, high porosity, and soft consistency are versatile biomaterials in many biomedical applications, including drug delivery, tissue engineering, regenerative medicine, and wound dressing. Compared to most synthetic biomaterials, and considering the mechanical behavior, they resemble the structures of the extracellular matrix and tissues; accordingly, they are becoming hotspots in modern biomedical research (Caló & Khutoryanskiy, 2015; Wahid et al., 2020; Ye et al., 2020). Hydrogels of natural origin, bio-hydrogels, which are mainly extracted from plants, are becoming more attractive due to their inherent advantages, such as hydrophilicity, biocompatibility, and non-toxicity. Aloe vera (AV) gel with intrinsic healing properties, anti-inflammatory, antimicrobial, and anti-septic activity, has been traditionally used to treat wounds (Bialik-Wąs et al., 2020; Thomas et al., 2020). The polysaccharides found in AV gel, mainly acemannan, can bind to the cell membrane and plasma proteins and accelerate the wound healing process by increasing collagen synthesis. Furthermore, these polysaccharides are involved in hyaluronic acid and hydroxyproline production in fibroblasts, which can significantly reconstruct the extracellular matrix. Additionally, the presence of barbaloin, aloetic acid, and isobarbaloi in AV gel is proven to provide significant antibiotic and antimicrobial properties and give an analgesic effect, which can relieve pain during a healing process (Ghorbani et al., 2020; Yin & Xu, 2020). Nevertheless, the main drawback of AV gel is its relatively low mechanical stability restricting its application in certain biomedical applications. It has been shown that one way to introduce mechanical anisotropy into hydrogels is to incorporate stiffer elements with a high aspect ratio within the hydrogel structure (Fourmann et al., 2021). As the most abundant natural polymer, cellulose has been widely used as reinforcement in different fields, such as biomedicine areas, food packaging, biocomposites, etc., since it possesses many useful material properties, including biocompatibility, biodegradability, modifiable surface chemistry, and good mechanical strength (Ajdary, Tardy, et al., 2020; Chao et al., 2020; Jack et al., 2019; Pillai et al., 2021; Trifol et al., 2021). Its nanoscale form, nanocellulose, which could be found in the forms of cellulose nanofibrils (CNFs), 2,2,6,6-tetramethylpiperidin-1-oxy-oxidized cellulose nanofibers (TEMPO-CNFs or TOCNFs), cellulose nanocrystals (CNCs), and bacterial cellulose (BC), presented a multifaceted range of biomedical

* Corresponding author.
E-mail address: jukka.seppala@aalto.fi (J. Seppälä).
[1] These authors had the same contribution.

https://doi.org/10.1016/j.carbpol.2021.118114
Received 10 March 2021; Received in revised form 14 April 2021; Accepted 19 April 2021
Available online 24 April 2021

applications (Ajdary et al., 2019; Ajdary, Ezazi, et al., 2020; Darpentigny et al., 2020; Tehrani et al., 2016).

On the other hand, over the past decade, 3D printing, a method of making three-dimensional objects in a digitally controlled layer-by-layer manner, has become increasingly popular owing to its exciting advantages such as low material consumption, customizable object geometry, cost-effective, and rapid, customizable on-demand fabrication (Li et al., 2020; Yang, An, et al., 2020). Several techniques, including contact (flexographic, gravure, offset, screen) and non-contact (inkjet and aerosol) printing, have been frequently employed to print flexible substrates. Due to the low ink consumption, low cost, and simplicity of changing digital print patterns, direct ink writing (DIW) is gaining much attention for hydrogel printing (Ajdary, Tardy, et al., 2020; Tehrani et al., 2016). However, it is restricted to the viscoelastic properties of the ink. Hydrogels for 3D printing need to be fluid enough to be pressed through the nozzle during printing and be viscous during printing to be deposited in 3D patterns and retain the 3D structure after printing. On top of that, they should possess shear-thinning or stimuli-responsive properties to make 3D printing possible. Shear-thinning hydrogels can be printed under shear force and recover mechanical properties after extrusion (Liu et al., n.d.; Yang, Lu, et al., 2020).

The main hypothesis of this research was to investigate the printability of the blends of two polysaccharides, aloe vera gel and cellulose nanofibrils, that had not been studied before. The viscoelastic properties of the pure AV, TOCNF, and composite hydrogels were studied thoroughly to investigate their printability. The lattice geometries were printed precisely with high-shape fidelity, physically were cross-linked using calcium chloride, and their physio-mechanical characteristics were evaluated.

2. Materials and methods

2.1. Materials

Fresh Aloe vera (AV) plant leaves were purchased, and the gel was extracted. Calcium chloride, sodium bromide, sodium hypochlorite, and sodium hydroxide were provided from Sigma. Phosphate buffered saline (PBS, pH = 7.4) was purchased from Alfa Aesar. Milli-Q water was purified by a Millipore Synergy UV unit (18.2 MΩ cm) and was utilized throughout the experiments.

2.2. Preparation of TOCNF

Nanocellulose was produced by processing the never-dried birch fibers with TEMPO-mediated oxidation (2,2,6,6-tetramethylpiperidine-1-oxyl). Birch fibers were immersed in milli-Q water, followed by the addition of 0.013 mmol/g TEMPO and 0.13 mmol/g sodium bromide. Sodium hypochlorite (5 mmol/g) was added to the suspension, and the pH was adjusted to 10 by the addition of sodium hydroxide in 0.1 M concentration. The mixture was kept at room temperature and stirred for approximately 6 h. The resulted fibers were washed with deionized water until a neutral pH was achieved. The fibers were further fibrillated with a microfluidizer (M-110P, Microfluidics In., Newton, MA) with one pass at a pressure of 1400 bar. The translucent and viscose hydrogel was concentrated to 1.5 wt% by water evaporation under stirring at room temperature.

2.3. Preparation of 3D printing biomaterial inks

Although aloe vera gel has been used for wound treatment and also as a flavoring component in foods and as an additive in cosmetics, it has been reported that the aloe vera leaf extract might show a carcinogenic activity in rats (Guo & Mei, 2016); therefore, in the current study, the gel inside the fresh aloe vera leaf was carefully extracted to avoid the presence of any material from the cuticle and then mechanically stirred for 5 min to obtain the uniform gel. Afterward, it was filtered using a cotton filter to remove some solid impurities. The filtered gel was centrifuged for 10 min at 7000 rpm to sediment residual impurities. The purified AV gel was frozen at −40 °C for 24 h and dried at −40 °C for 48 h using a freeze dryer. The dried AV powder was dissolved in distilled water at ambient temperature for an hour to obtain 1.5 wt% uniform hydrogel. Different weight ratios of AV (1.5 wt%) and TOCNF (1.5 wt%) hydrogels, including 100/0, 75/25, 50/50, 25/75, and 0/100, mechanically mixed and homogenized thoroughly using an IKA Ultra Turrax T25 digital homogenizer at room temperature to obtain completely uniform ink. The inks were codded as A100T0, A75T25, A50T50, A25T75, and A0T100, respectively, and were centrifuged to remove any bubbles before use for 3D printing.

2.4. Direct ink writing and crosslinking

A BIOX bioprinter (CELLINK, Sweden) equipped with a pneumatic printhead was employed to print the 3D CAD model designed in Tinkercad. The 3 ml clear pneumatic syringe and 20-gauge sterile blunt needle (630 μm tip diameter) were utilized to print the samples. All structures were printed on the plastic petri dish (60 mm diameter). For the swelling, weight loss, and porosity tests, disc-shaped samples with a diameter of 15 mm were printed, while for the compression and rheology tests, the diameter was selected as 25 mm. The number of layers in all printed samples was fixed at five, and printing was done with an infill density of 100%. Furthermore, a grid lattice structure was printed to illustrate the hydrogels' ability to be printed on complex geometries. The printed samples were frozen overnight and lyophilized at −40 °C for 48 h. Hydrogels can be crosslinked either chemically by covalent bonds or physically by hydrogen bonding, hydrophobic interactions, and ionic complexation. However, to avoid toxicity related to chemical crosslinking agents, physically cross-linked gels might be preferred (Shefa et al., 2020). Accordingly, the lyophilized 3D-printed samples were soaked in calcium chloride solution (1 M) for two h for crosslinking, washed several times with distilled water to remove any unreacted crosslinker solution, and lyophilized again at −40 °C.

2.5. Characterizations

Rheology. Rotational rheometer experiments were carried out using an Anton Paar rheometer (Anton Paar MCR 301 GmbH, Austria) with parallel plates (PP25 and CP25 geometries) at the different gap values to study the rheological behavior of ink and printed freeze-dried sample. The apparent shear viscosity of the inks was monitored by increasing the shear rate from 0.01 to 100 s^{-1} using CP25 geometry at a fixed gap of 49 μm. Furthermore, the ink and freeze-dried printed sample's linear viscoelastic range was determined employing PP25 geometry through a strain sweep of 0.01 to 100% at a fixed frequency of 10 rad·s^{-1} and the fixed gap of 1 mm and 3 mm, respectively. Afterward, a dynamic frequency sweep was conducted between 0.1 and 100 rad·s^{-1} on the ink and freeze-dried 3D-printed sample using a PP25 parallel plate geometry within the linear viscoelastic region (a constant strain of 0.1%). The dynamic mechanical properties, including the storage modulus (G′) and loss modulus (G″), were obtained as a frequency function. Furthermore, the tensile modulus (E) of the printed samples was calculated using Eq. (1), in which ν is the Poisson ratio. Since the mechanical behavior of the swollen sample can be considered similar to that of rubber-like materials, the value of ν was selected as 0.5 (Baniasadi et al., 2015). All measurements were performed at 25 °C.

$$E = 2G'(1 + 2\nu) \quad (1)$$

Zeta potential. To evaluate the surface charge, all inks were diluted to 0.1 wt% in 5×10^{-3} M sodium chloride and utilized to measure the ζ-potential using a dip cell on a Malvern Zetasizer ZS (Malvern Panalytical, UK).

Shrinking behavior of the 3D-printed sample. The extent of

shrinkage in the samples was reported by monitoring the geometrical changes in the wet and dry conditions, e.g., freeze-dried and room temperature dried (RT-dried). The printed sample volumes before (V_w) and after (V_d) drying were measured, and the following equation was used to calculate the shrinkage.

$$\text{Shrinkage}\ (\%) = \frac{V_w - V_d}{V_w} \times 100 \quad (2)$$

Scanning electron microscopy. SEM was performed with a Zeiss Sigma VP microscope (Zeiss, Germany) at the voltage of 2–4 kV. The freeze-dried 3D printed sample was sputtered with a 4 nm layer of the gold-palladium alloy (LECIA EM ACE600 sputter coater) before taking the image.

Swelling ratio and weight loss. The freeze-dried 3D sample was thoroughly dried in a vacuum oven at 40 °C overnight. Then it was weighed (m_0) and soaked in PBS solution at room temperature. It was taken out at specified times, and the surface water was removed using tissue paper and weighted immediately (m_s). The swelling ratio (SR) was calculated using Eq. (3). Each measurement was repeated three times, and the mean value ± error of the mean was reported.

$$\text{SR}\ (g/g) = \frac{m_s - m_0}{m_0} \quad (3)$$

The weight loss (WL) was calculated using the previously presented SR measurement method with specific differences. The soaked sample was taken out at the defined periods, thoroughly vacuum dried at 40 °C, and then weighted (w_d). The WL was calculated using Eq. (4). Each measurement was repeated three times, and the mean value ± error of the mean was reported.

$$\text{WL}\ (\%) = \frac{m_0 - m_d}{m_0} \times 100 \quad (4)$$

Porosity. The porosity of the freeze-dried printed structures was evaluated by the ethanol saturation method (Shahini et al., 2013). The sample with defined geometry (disc shape with a diameter and height of 15 mm and 3 mm, respectively) were immersed in pure ethanol for 48 h, the change in the weight was monitored, and the porosity (Φ) was calculated by using Eq. (5).

$$\Phi(\%) = \frac{m_{sat} - m_d}{\rho V} \times 100 \quad (5)$$

where m_{sat} demonstrates the weight of the sample saturated with pure ethanol, m_d is the dry mass, ρ is the density of the ethanol, and V is the apparent volume of the structure. The presented values were the average of three to five replicates ± error of the mean.

Fourier transform infrared (FTIR) spectrometry. FTIR spectra were recorded using a PerkinElmer FTIR with an ATR instrument in a reflection mode. Spectra were recorded between 4000 and 500 cm^{-1} at a 4 cm^{-1} resolution, and 32 scans were accumulated.

Thermogravimetry analysis. The TGA was performed using a TA Instruments TGA Q500 at a temperature range of 30 to 800 °C with a heating rate of 10 °C.min^{-1} under a nitrogen atmosphere.

Compression test. The compression test was done using a TA Instruments Model Q800 in compression mode at humidity control conditions. The cross-linked lyophilized printed sample was soaked in PBS solution 24 h before the test. Afterward, it was equilibrated at 25 °C for 2 min, then subjected to the controlled force with a rate of 0.1 N.min^{-1} up to 18 N at pre-load of 0.001 N. The compressive stress and strain curve, compression modulus, and stress at 30% strain, were reported for all samples.

3. Results and discussion

The employed pure AV, TOCNF, and composite hydrogels are depicted in Fig. 1. All gels were transparent, and the mixed ones had a very uniform feature indicating good compatibility between two polymeric phases. Fig. 1 furthermore illustrates the surface charge of the pure and composite inks. All hydrogels revealed approximately the same negative surface charge due to the presence of carboxylic groups in their structures. This amount of negative surface charge can guarantee the improved dispersion stability of the ink in water, a considerable decrease in hydrogel aggregation, and enhanced stability after extrusion (Ajdary et al., 2019; Wei et al., 2016).

3.1. Rheological behavior of the inks

Several research studies revealed that a shear-thinning hydrogel ink, which exhibits a viscoelastic response to applied pressure, can be extruded from a nozzle to directly deposit the gel to fabricate a 3D object. They furthermore reported that the viscosity should be high enough because the small viscosity induces poor shape fidelity during 3D printing and causes the collapse of the shape (Liu et al., 2020; Smith et al., 2018; Wang, Liu, et al., 2021). Therefore, the rheological performances of all inks were studied. Fig. 2a illustrates viscosity-shear rate curves, where the viscosity curves were smooth with no mutation, indicating that the inks were stable enough (Wei et al., 2020). The viscosity of all inks was within the reported range suitable for the extrusion of hydrogels, which may afford excellent shape fidelity when printing. For instance, the viscosity at a low shear rate (0.01 s^{-1}) was between 2800 and 4400 mPa·s^1, depending on the TOCNF concentration. This value is in good agreement with those reported for TEMPO-oxidized bacterial cellulose/alginate inks (Wei et al., 2020) and for pure inks at given concentrations of cellulose (Jiang et al., 2021). Furthermore, all inks revealed a similar shear-thinning behavior, wherein the viscosity dropped approximately two orders of magnitude as the shear rate increased from 0.01 to 100 s^{-1}. This behavior can be advantageous for 3D printing since it guarantees the smooth flow of hydrogels from a nozzle during DIW printing and enables efficient flow through fine deposition nozzles (Siqueira et al., 2017; Smith et al., 2018).

The shear strain must be within the linear viscoelastic area during material property constant measurements, so linear viscoelastic zone measurements of the fracturing fluids should be conducted prior to the viscoelastic measurements (Zhang et al., 2019). Accordingly, the strain

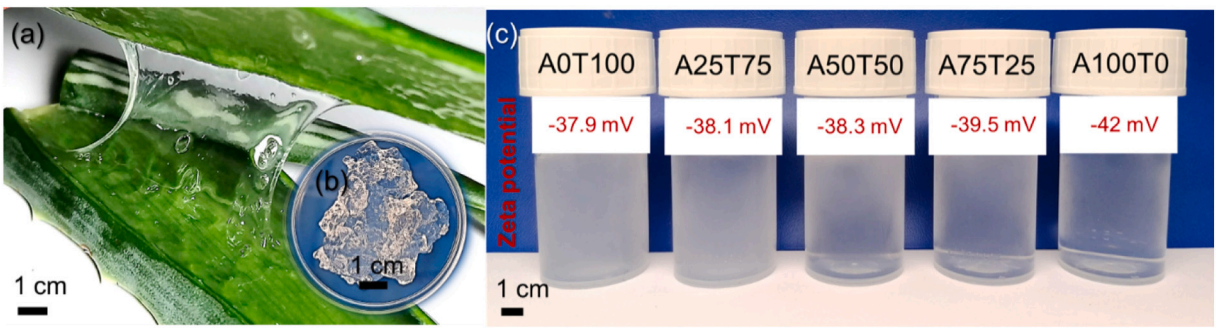

Fig. 1. (a) The AV gel, (b) TOCNF, and (c) AV/TOCNF composite inks and their surface charges.

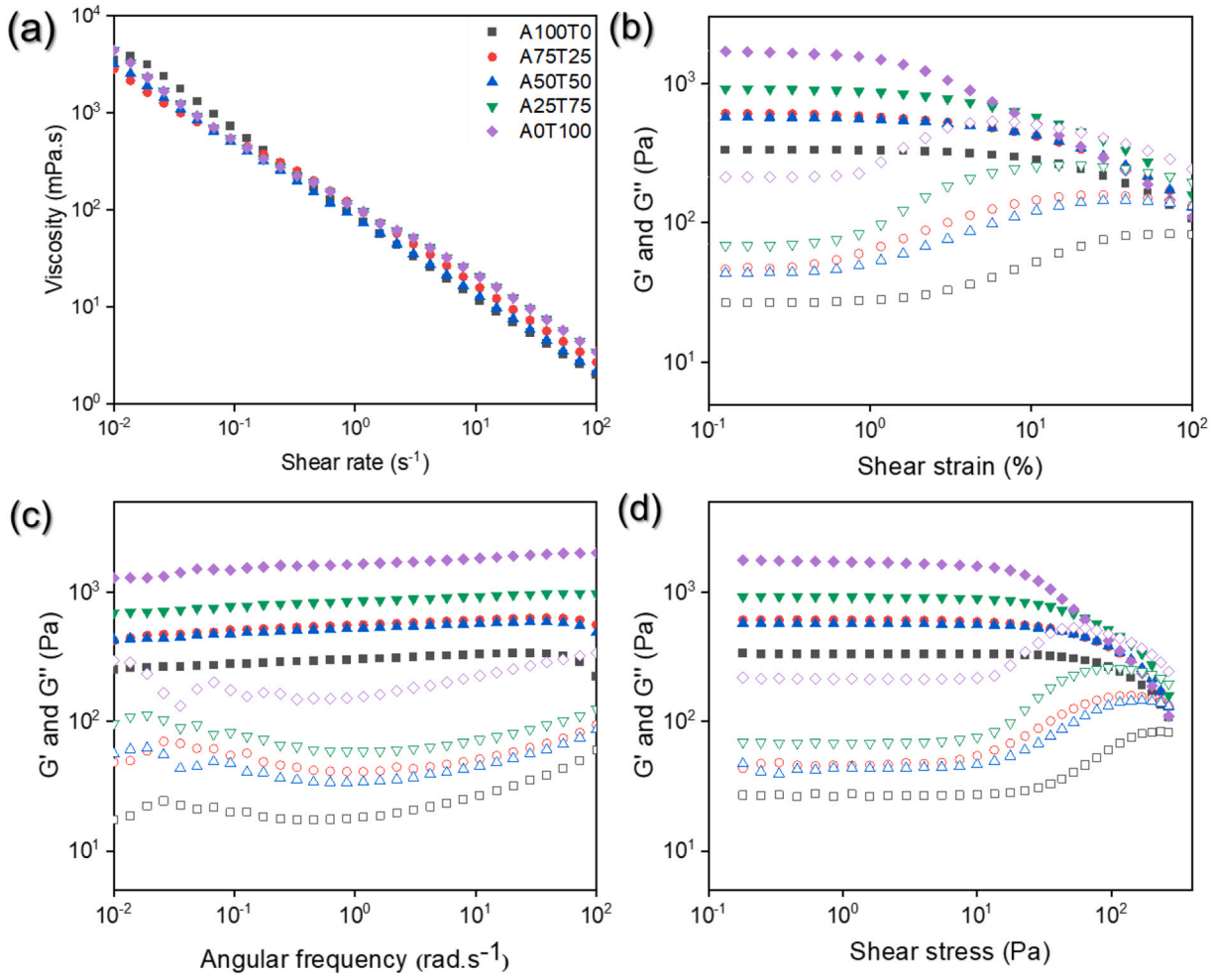

Fig. 2. (a) Viscosity curves versus shear rate ($\dot{\gamma}$), (b) strain-sweep at a fixed frequency of 10 rad·s^{-1}, (c) frequency-sweep at a fixed shear strain of 0.1%, and (d) shear stress-sweep at 25 °C. In figures b, c, and d, the solid and blank symbols indicate G′, and G″, respectively.

sweep test was performed on all inks in the shear strain rate of 0.01 to 100 rad·s^{-1}. The results are summarized in Fig. 2b. A100T0 sample illustrated plateau value at shear strain rate less than 10%, indicating the linear viscoelastic behavior region of pure AV gel. This region decreased with an increase in the TOCNF content due to the formation of more robust polymer networks, which are shown to be collapsed at smaller deformations (Moud et al., 2021). The wider viscoelastic region could be advantageous for soft materials like hydrogels since the wide-range linear viscoelastic hydrogels are highly demanded in diverse applications (Ma et al., 2020). Eventually, 0.1% was considered a safe value for the strain to ensure that the measurements were in the viscoelastic region. The oscillatory measurements at a low strain of 0.1% were conducted to assess the viscoelastic properties of the inks. Fig. 2c depicts the trend of storage and loss moduli over frequency inside the linear viscoelastic region.

The storage modulus was always higher than the loss modulus, indicating a soli-like or network-like behavior; furthermore, both moduli increased upon increasing TOCNF content, attributed to the uniform dispersion of high aspect ratio nano and microfibrils cellulose, reinforced the 3D hydrogel structure. This improvement can help the ink better preserve its structure after extruding out from the nozzle during 3D printing. The storage modulus values in the current study were measured to be in the range between 300 and 2000 Pa, depending on TOCNF content. These values are similar to those reported for pure cellulose inks (Jiang et al., 2021) and cellulose nanocrystal/pectin composite hydrogels (Ma et al., 2021).

To guarantee the successful direct writing of the ink, in addition to shear-thinning behavior, the ink should be flow through the nozzle under the applied pressure. In other words, the yield stress (τ_y) of the ink should be lower than the maximum shear stress generated within the nozzle (τ_{max}). When τ_{max}, originated from the pneumatic pressure during printing, is not high enough to overcome τ_y, a plug flow regime develops, leading to an unyielded ink region whose velocity remains constant. Under these conditions, hydrogels would not be expected to print (Ma et al., 2021; Siqueira et al., 2017). To obtain τ_y of the inks, the stress sweep test was done at a fixed frequency of 10 rad·s^{-1} (Fig. 2d). As can be seen, G′ was higher than G″ at low stress rates, while G″ passed over G′ at high stress values. In other words, all hydrogels first exhibited predominantly elastic behavior at low shear rates (G′ > G″), then revealed definite dynamic yield stress (G′ = G″) with further increase in the shear rates, and finally showed viscous behavior (G′ < G″). The stress value at intercession points was considered as yield stress of the ink. On the other side, since the residence time of the ink in the nozzle during extrusion was relatively short, τ_{max} was considered the shear rate at the nozzle wall. It was calculated using the following equation (Siqueira et al., 2017).

$$\tau_{max} = \frac{\Delta P.r}{2L} \quad (6)$$

where ΔP is the maximum pressure applied at the nozzle, and r and L are the nozzle radius and the nozzle length, respectively. The maximum applied pressure during 3D printing was 40 × 10^3 Pa, and the nozzle

diameter and the nozzle length were 630×10^{-6} m and 2.5×10^{-2} m, respectively. Accordingly, the maximum shear stress (τ_{max}) at the nozzle wall was 252 Pa, which was higher than the yield stress of all samples (Fig. 2d), suggesting that all inks could be printed.

3.2. 3D-printed construct and shrinkage study

Two main challenges in the 3D printing of hydrogel precursors are shape fidelity and integrity, as they can influence the overall performance of 3D structures (Curti et al., 2021). Fig. 3 illustrates the lattice structures composed of five layers, printed with A100T0, A50T50, and A0T100 inks. A flower that was printed using A50T50 ink is also demonstrated in Fig. 3. All inks had excellent flowability under the printing conditions due to their shear-thinning behavior and lower yield stress values than the applied stress on the nozzle tip. Moreover, they were printed successfully with high precision and fair resolution using the 20 G needle. No evidence of the common challenges in DIW, such as needle clogging and liquid spreading (Luo et al., 2018), was observed. On top of that, each layer never deformed or collapsed and revealed excellent self-supporting characteristics during and after printing, even in the A100T0 sample (pure aloe vera), suggesting that the ink recovered its relatively high viscosity in quite a short time after being sheared in the nozzle (Coffigniez et al., 2021). Overall, the observed results, which were in line with the rheological investigations, confirmed that the developed inks had good printability with a fair resolution.

Preservation of the three-dimensional structure after printing is a crucial parameter in direct ink writing of hydrogels since they retain a considerable amount of water in their structure (compared to the weight of dry polymer), whose loss may cause severe dimensional changes. The dimensional changes after drying, which play an essential role in the structure, density, porosity, rheology behavior, and mechanical property of the resulting structures, are usually quantified in hydrogels by measuring the shrinkage (Fan et al., 2018). Accordingly, the shrinkage behavior of the 3D-printed samples was evaluated by monitoring their volume changes after drying. Fig. 3 demonstrates some 3D-printed samples (A100T0, A50T50, and A0T100) after drying. The results of

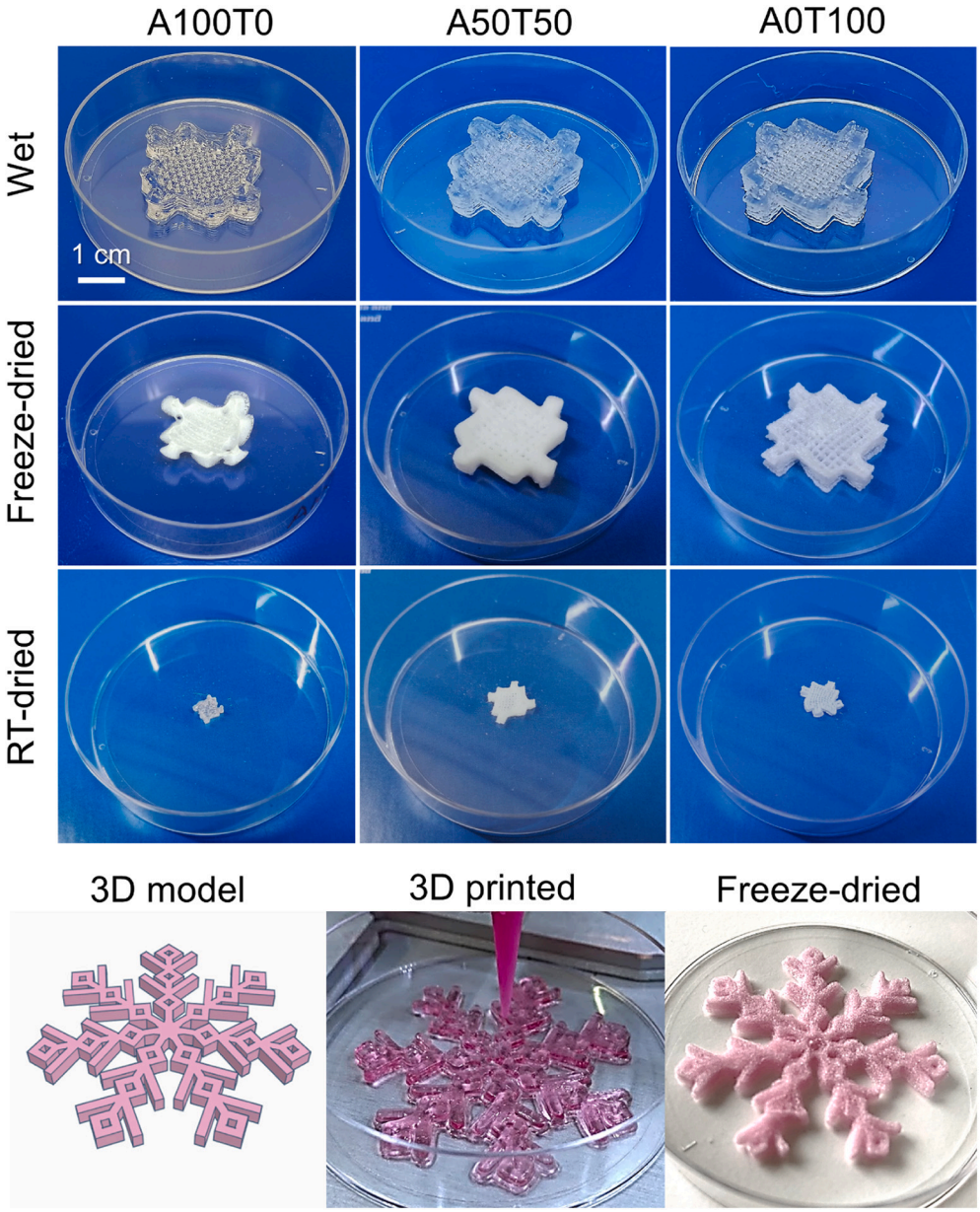

Fig. 3. 3D-printed structures before crosslinking (wet condition) and after crosslinking (freeze-dried and RT-dried). The follower was printed using A50T50 ink. For better illustration, an edible color was added to the ink.

the shrinkage measurement for RT- and freeze-dried samples are also summarized in Table 1. On one side, the freeze-dried samples retained the shape more effectively than the RT-dried ones, demonstrating the advantage of lyophilization to preserve the structure of the hydrogels even after removal of all the solvent (Li et al., 2017). The dramatic changes in the fidelity of the RT-dried samples could be due to the high water content captured in their structure (Lu et al., 2018). On the other side, the shrinkage decreased upon increasing TOCNF content due to uniform dispersion of the high aspect ratio nano and microfibrils cellulose (optical microscope images in Fig. S1) reinforced the 3D hydrogel structure and protected the shape from extensive shrinkage upon drying. Notably, the observed shrinkage was relatively higher than that reported for the cellulose-reinforced hydrogels (Jiang et al., 2020), which could be due to the inherently low mechanical stability of the aloe vera gel and the relatively high water uptake capacity (up to eight times of the sample dry weight). It is worth notifying that because the A100T0 sample had suffered appreciable volume shrinkage, it was not suitable for the mechanical and rheology tests; therefore, it was subjected neither to compression nor frequency sweep tests.

3.3. Microstructure and porosity

The microstructure of the freeze-dried samples before and after crosslinking is provided in Fig. 4 and Fig. S2. The A100T0 sample demonstrated completely homogeneous and non-porous geometry before crosslinking, which could be due to the collapse of the pores during freeze-drying that arose from its relatively high shrinkage and poor mechanical properties. It could also be attributed to many active substances, including mucopolysaccharides and polysaccharides, in its structure that penetrated into the free spaces of the gel and consequently disappeared the porosity (Bialik-Wąs et al., 2020). On the other side, the A0T100 sample illustrated a porous structure; however, the pores were large and had poorly defined internal walls. The A50T50 sample presented a spongy and porous structure, better-defined pores, thinner walls, and smaller pore sizes. This might be due to TOCNF acted as a crosslinked agent between carboxylic groups of AV, and excess of TOCNF worked as bridge lines between AV gel (Angulo et al., 2019). The better-defined pores in the A50T50 sample than A0T100 could be due to the formation of a more relaxed polymer network in the presence of aloe vera (Bialik-Wąs et al., 2020). In all samples, the cross-linking changed the microstructure significantly. The microstructure became more complicated with a smaller pore size attributing to strong hydrogen-bonding interactions established between carboxylic groups of AV and TOCNF with Ca^{2+} ions (Li et al., 2017). Finally, no evidence of two-phase morphology was observed in the SEM images confirming good compatibility between two polymer phases.

The porosity of all the freeze-dried cross-linked samples is summarized in Table 1. It is known that the shrinkage of the hydrogel reduces the pores (Kopač et al., 2020); accordingly, the A100T0 sample that had the highest shrinkage revealed the lowest porosity. However, the porosity of the other samples did not show significant differences. The high porosity of the samples (more than 80%) made them interesting candidates for biomedical application as they can absorb the exudates and easily transport the liquids, gas, and nutrients. Furthermore, they can easily absorb culture medium to facilitate cell migration, adhesive, and proliferation into and on their porous structures (Abdel-Mohsen, Frankova, et al., 2020; Shefa et al., 2020).

Table 1
Sample physical characteristics.

Sample	Shrinkage, freeze-dried %	Shrinkage, RT-dried %	Porosity[a] %	Swelling[a,b] g/g	Weight loss[a,b] %
A100T0	46 ± 2.8	92 ± 4.1	84 ± 2.1	8.5 ± 0.8	3.2 ± 0.4
A75T25	31 ± 2.2	91 ± 3.3	95 ± 2.6	21 ± 1.3	2.7 ± 0.3
A50T50	24 ± 0.9	86 ± 5.3	94 ± 1.4	36 ± 2.3	2.4 ± 0.2
A25T75	19 ± 1.1	84 ± 3.7	94 ± 1.1	46 ± 1.8	1.8 ± 0.2
A0T100	12 ± 0.8	83 ± 4.1	92 ± 3.2	30 ± 2.1	1.7 ± 0.07

[a] Freeze-dried sample.
[b] After 24 h.

3.4. Swelling and weight loss

The swelling rate determined the exchange of nutrients and metabolites by the hydrogel. Moreover, it provides 3D structures favorable for cell infiltration and migration (Nazarnezhada et al., 2020; Zhang et al., 2020). Accordingly, the swelling behavior of all freeze-dried printed samples was monitored in PBS solution for 72 h. Fig. 5a illustrates the swelling values (g/g) for the samples. Furthermore, the digital photos of samples before and after swelling and the swelling values after 24 h are provided in Fig. 5c and Table 2, respectively. All samples revealed high-water uptake capacity, which stabilized after 6 h. This relatively high-water absorption capacity was attributed to the hydrophilic groups existing in the AV and TOCNF structure, which quickly absorbed water molecules in the environment and increased the swelling rate over time. Moreover, it could be due to the high porosity of the samples (Khodabakhshi et al., 2019; Zhang et al., 2020). After equilibrated values, the swelling ratio did not reduce in all samples, suggesting an enhanced physical strength and well-preserved three-dimensional pore structure due to the hydrogen bonding established by Ca^{2+} ions inside the hydrogel structure. Nevertheless, as Fig. 5c presents, the samples with higher loading of TOCNF were more stable 24 h after swelling due to the support provided by high aspect ratio micro- and nano-size fibrils. On the other side, the swelling ratio increased dramatically upon increasing the TOCNF content attributed to the hydrophilic nature of cellulose and its carboxylic acid functionalities on the fibril surface (Dai et al., 2019). Surprisingly, composite samples revealed a higher swelling ratio than the pure TOCNF sample (A0T100), which could be explained by their better-defined and smaller pore sizes that increased the free volume for accommodating the water entering the gels (Dey et al., 2015). It is noteworthy that the measured swelling ratio in the current study was relatively higher than that reported for the hydrogels in the literature. For instance, it has was measured to be around 2 g/g for aldehyde-functionalized cellulose/chitosan hydrogels (after two h) (Abou-Yousef et al., 2021) or 3 (g/g) for carboxymethyl cellulose/poly-N-isopropylacrylamide composite hydrogels (after 24 h) (Su et al., 2020). The relatively high water uptake capacity might be advantageous for certain biomedical applications, such as wound dressing (Nazarnezhada et al., 2020). On the other hand, the water uptake is associated with extensive dimensional changes after drying.

The weight loss of all the cross-linked lyophilized 3D-printed samples was studied over 72 h. The results are introduced in Fig. 5b and Table 2. All the hydrogel formulations demonstrated low weight loss over time due to successful crosslinking that preserved the integrity of the polymer network (Hu et al., 2019). However, the samples with a higher content of TOCNF revealed slightly lower loss weight because the high crystalline structure nanocellulose undergoes degradation just under specific enzymatic, autocatalytic, or hydrolytic activities (Heinze, 2016; Łojewska et al., 2005). The relatively higher weight loss of pure AV gel (A100T0) could be to the week hydrogen bond interactions between the molecules, which easily dissolved in solution after swelling (Huang et al., 2020).

3.5. Rheological and mechanical properties of the lyophilized 3D-printed hydrogels

On the one hand, a hydrogel should possess significant mechanical properties to facilitate its handling. On the other hand, its mechanical properties should be within the appropriate reported ranges for the demanded applications. Accordingly, for investigating the elastic characteristics and mechanical performances, the freeze-dried 3D-printed

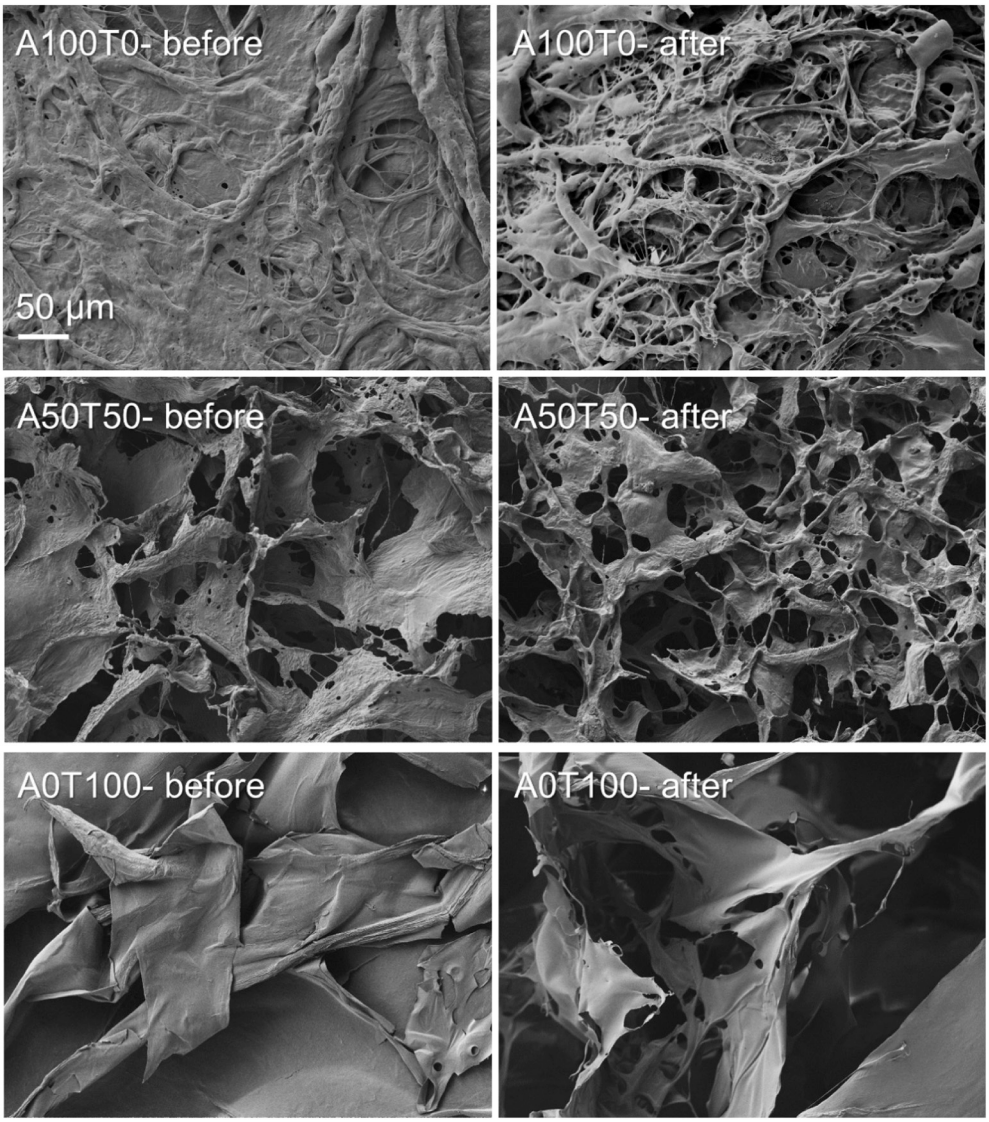

Fig. 4. The microstructure of the A100T0, A50T50, and A0T100 before and after crosslinking. The scale bar and magnification for all images are 50 μm and 500×, respectively.

samples were subjected to an oscillatory rheometry and compression test. First, a dynamic strain sweep test was applied to find the linear viscoelastic region. Fig. 6a shows the strain sweep test results. All samples revealed a linear behavior below the critical strain value (approximately 1%). However, after the critical value, the modulus gradually decreased, indicating a partial breakup of the gel (Das et al., 2015). Like the inks, the linear region was lower for the samples with higher TOCNF content. Accordingly, the strain of 0.1% was determined for all samples as the frequency test's strain value. The dynamic mechanical spectra (G′ and G″ moduli) of all samples at the aforementioned strain value are demonstrated in Fig. 6b. For all samples, G′ was higher than G″, indicating a gel-like or solid-like behavior in which the elastic and loss moduli were independent of frequency. The higher values of G′ suggested that interactions between cellulose nanofibers and hydrogen bond formation with water and adjacent polysaccharide portions were quite strong; thus, the network structures formed successfully, and it was kept stable under large deformations. In other words, the rearrangement of the network structure among the cellulose nanofibers and AV could not accommodate the strain in a timely fashion within a period of oscillation (Jia et al., 2019; Lu, Han, et al., 2020). A similar trend has been reported for TOCNF at higher fibrils concentrations (Alves et al., 2020; Czaikoski et al., 2020) and AV gel with a concentration of 0.2 to 1.6% (v/w) (Patruni et al., 2018). On the other side, G′ and G″ increased upon increasing TOCNF content, which could be explained by the orientation of cellulose nanofibrils under the high shear and extensional forces associated with passing through a nozzle (Fourmann et al., 2021). Of note that both storage and loss moduli of 3D-printed samples were approximately two orders of magnitude higher than what was reported for the ink (Fig. 2c), confirming the effect of freeze-drying and crosslinking on improving the hydrogels' stability (Bercea et al., 2019; Seo et al., 2020). The storage modulus was used to calculate the tensile modulus using Eq. (1). The results are summarized in Table 2. The tensile modulus was 4.95 ± 0.22 kPa for A100T0 and increased dramatically upon increasing the TOCNF content suggesting its reinforcing effect. The ideal hydrogel for tissue engineering applications should be compatible with the tissue's mechanical properties, e.g., to ensure its integrity while adhering to the tissue. On the one hand, the tensile modulus of the developed, printed structures matched those of soft tissues and human skin (Demeter et al., 2020; Xue et al., 2019). On the other hand, the measured values were in the range reported for the tensile modulus of bacterial cellulose-reinforced polyacrylamide/iota-carrageenan hydrogels (Hua et al., 2021), polyvinyl alcohol/lignosulfonate sodium hydrogels (Wang, Pan, et al., 2021), and collagen/hollow fiber/aloe vera hydrogels (Abdel-Mohsen, Abdel-Rahman, et al., 2020).

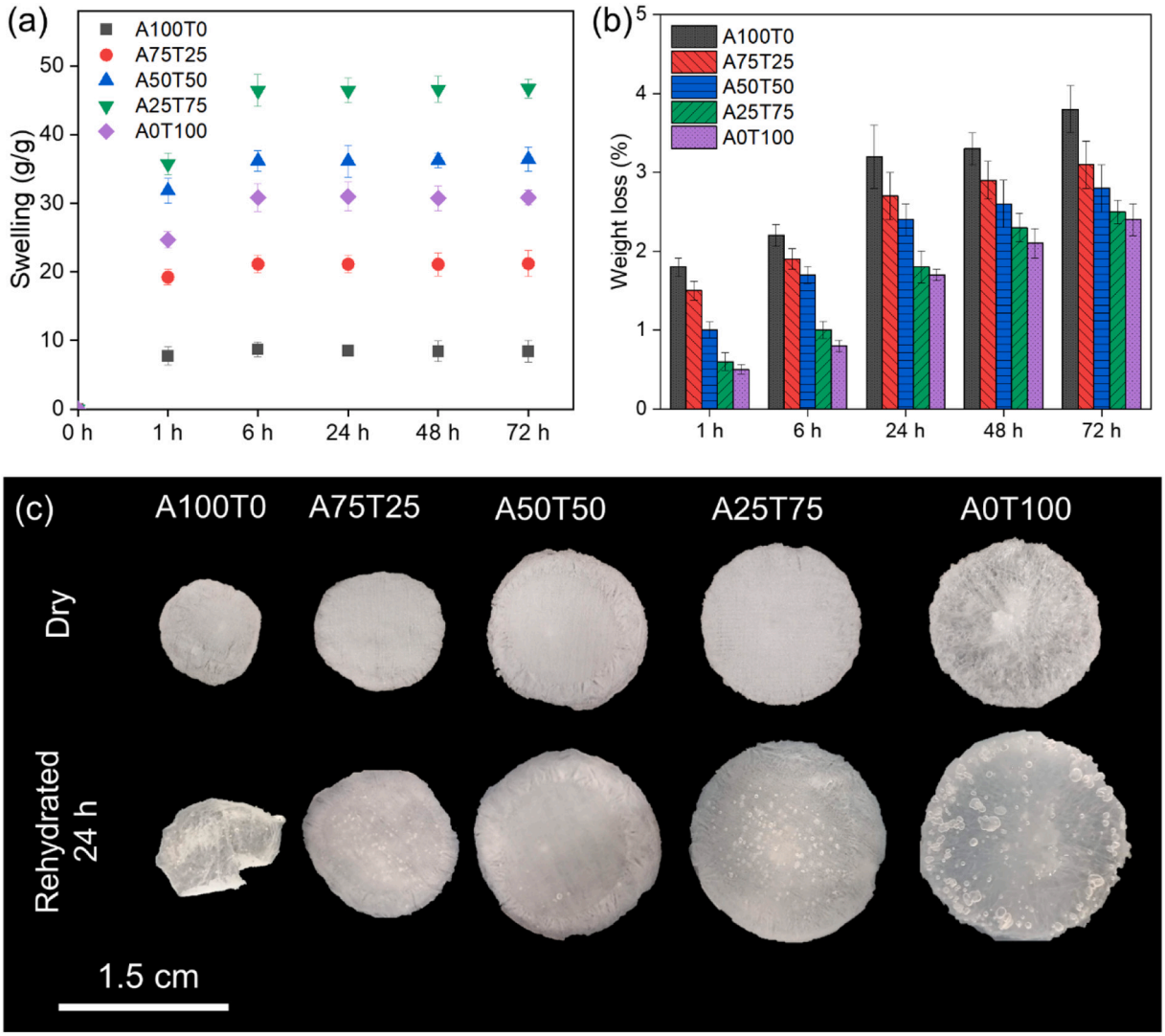

Fig. 5. (a) Swelling and (b) weight loss of the 3D-printed samples in distilled water. (c) The illustration of real sample swelling after 24 h.

Table 2
Mechanical properties of the lyophilized printed samples.

Sample	Tensile modulus (kPa)	Compression modulus[a] (kPa)	Compression stress[a] (kPa)
A75T25	4.95 ± 0.22	0.92 ± 0.03	0.18 ± 0.00
A50T50	8.96 ± 0.43	4.38 ± 0.17	1.23 ± 0.05
A25T75	52.33 ± 2.36	4.96 ± 0.22	1.90 ± 0.07
A0T100	73.44 ± 3.12	6.54 ± 0.32	3.06 ± 0.13

[a] At 30% strain.

The mechanical performances of the printed hydrogels were further investigated by measuring the compressive mechanical properties of specimens. Fig. 6c shows the compressive stress-strain curves of all 3D-printed samples. The compression modulus and stress at 30% strain are also provided in Table 2. Except for the A75T25 sample, the other hydrogels revealed excellent stability during the test, and none of them experienced breakage within the applied forces. Moreover, all samples revealed a soft and stretchable behavior with a high linear deformation range attributed to a large amount of water trapped in the hydrogel matrix (Yue et al., 2021). The compression modulus increased dramatically upon increasing the TOCNF content, from 0.92 ± 0.03 kPa in A75T25 to 4.96 ± 0.22 kPa in A25T75, suggesting the formation of a robust and strong structure by generating a large number of hydrogen bonds with aloe vera. The obtained values were in good agreement with what has been reported for hydrogels used in soft tissue engineering applications (0.3–220 kPa) (Kambe et al., 2020). Furthermore, introducing TOCNF into the hydrogel led to a significant increase in the compression strength at 30% strain, from 0.18 ± 0.00 kPa in A75T25 samples to 1.90 ± 0.07 kPa A25T75. It is worth notifying that all samples deformed permanently during the test and could not recover, which could be explained by the absence of any covalent bonds during the gel formation, which made it difficult to recover their initial state (Lu, Yang, et al., 2020).

3.6. Chemical and thermal characterization

The FTIR spectra and TGA/DTG thermograms were employed to confirm the presence of two components (aloe vera and TOCNF) in composite hydrogels. Fig. 7a illustrates the FTIR spectra of the printed samples before and after crosslinking. The A100T0 sample (pure AV) presented a sharp peak at 3670 cm^{-1} assigned to the —OH groups of polysaccharide, a peak at 2900 cm^{-1} attributed to C—H stretching, a peak at 1410 cm^{-1} due to the symmetric deformation of —CH_2, and a sharp peak at 1060 cm^{-1} corresponded to the C—O skeletal vibrations (Abdel-Mohsen, Frankova, et al., 2020). On the other side, the A0T100 (TOCNF) revealed a sharp and a broad peak respectively at 3650 cm^{-1} and 3320 cm^{-1} attributed to O—H stretching, a peak centered at 2900

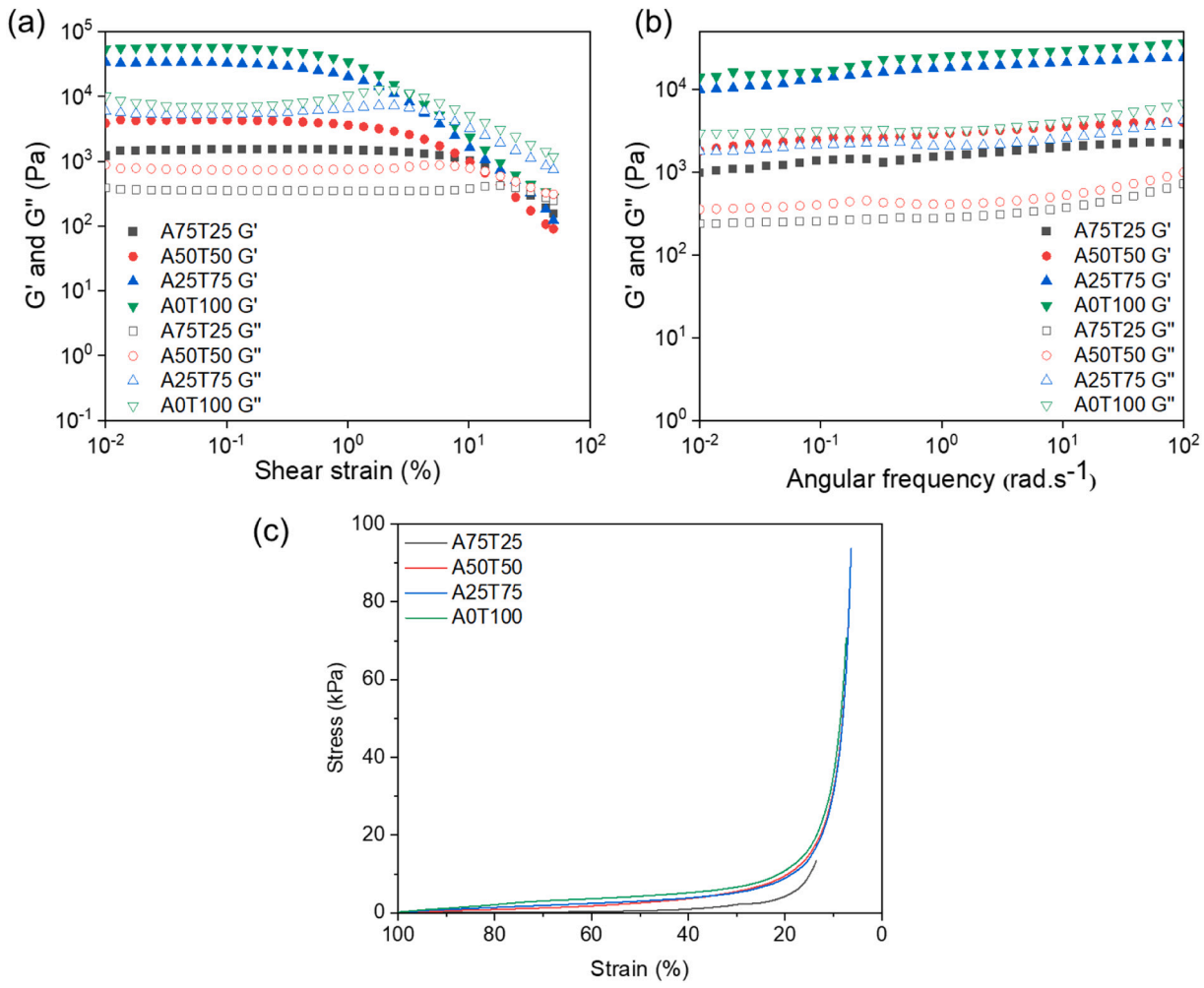

Fig. 6. (a) Strain-sweep test at a fixed angular frequency of 10 rad·s^{-1}, (b) frequency-sweep test at a fixed strain rate of 0.1%, and (c) compression stress-strain curves.

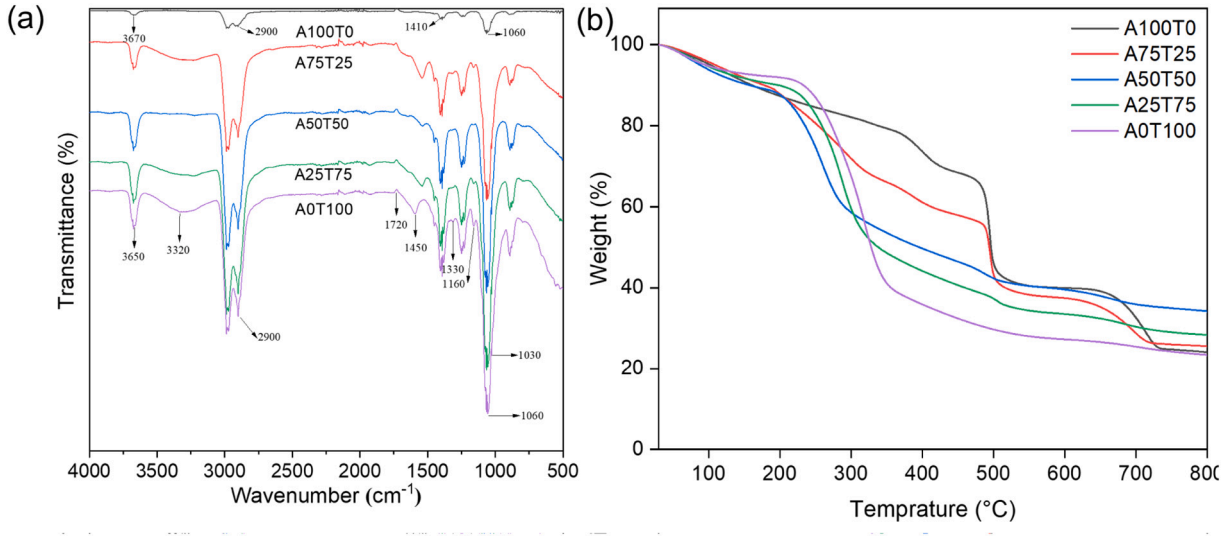

Fig. 7. (a) The FTIR spectra and (b) TGA thermograms of the lyophilized 3D-printed samples after crosslinking.

cm^{-1} corresponded to hybridized C—H stretching, and a peak at 1720 cm^{-1} assigned to the carbonyl groups (—COOH) resulted from cellulose TEMPO-mediate oxidation (Coseri et al., 2015). Furthermore, the peaks at 1450 cm^{-1}, 1330 cm^{-1}, 1160 cm^{-1}, 1060 cm^{-1}, and 1030 cm^{-1} were due to the symmetric deformation of —CH_2, the —OH in-plane bending, the asymmetric vibration of the C—O—C (bridge) linkage in cellulose,

the bending of the C—O—C bond in the pyranose ring and the C—O skeletal vibrations, respectively (Santmarti et al., 2020). All AV and TOCNF characteristic peaks were repeated in the composite samples (A75T25, A50T50, and A25T75), which could confirm the presence of two components in these samples. It is worth noting that no new peaks were detected by comparing the FTIR spectra of the 3D-printed samples before (Fig. S3a) and after crosslinking (Fig. 7a). It might confirm physical crosslinking formation through intermolecular hydrogen bonds between calcium ions and polysaccharide chains (Silva et al., 2019).

The presence of each component in the mixed samples after cross-linking was further investigated using TGA/DTG thermograms. Fig. 7b presents the TGA thermograms of all the cross-linked lyophilized printed samples. The corresponding derivatives of TG curves (DTG) are also provided in Fig. S3b. The pure AV and TOCNF samples revealed different thermal degradation behavior. The A100T0 sample demonstrated three mass loss stages. The first mass loss occurred at less than 200 °C, attributed to the dehydration of physically adsorbed and hydrogen bond-linked water, the second mass loss, which was happened between 200 and 400 °C, was due to the thermal polymer degradation, and the third stage between 400 and 700 °C corresponded to the carbonization of material (Aghamohamadi et al., 2019). On the other side, the A0T100 sample showed a minor mass loss at less than 100 °C assigned to bonded water evaporation in cellulose. Furthermore, it presented a significant mass loss between 250 and 400 °C (DTG peak at 320 °C), attributed to the depolymerization and degradation of hemicellulose glycosidic linkages (Jankowska et al., 2018; Onkarappa et al., 2020). In the composite samples (A75T25, A50T50, and A25T75), all aforementioned thermal degradation regions for pure AV and TOCNF were observed. Their DTG curves (Fig. S3b) illustrated four peaks, one at around 300 °C corresponded to the cellulose portion, and three at around 400, 500, and 700 °C attributed to the presence of AV. The first peak intensity increased by reducing TOCNF content, while it was decreased for three other peaks. Altogether, the TGA/DTG curve could confirm the presence of TOCNF and AV in the cross-linked lyophilized 3D-printed samples.

Since its first introduction, 3D printing has become an increasingly explored innovation technology, and research in this field has grown significantly over the past decade (Al-Dulimi et al., 2020; Li et al., 2020). Furthermore, the application of natural hydrogels in biomedical applications, including drug delivery, wound dressings, tissue engineering scaffolds, etc., has received extensive attention (Du et al., 2019). Accordingly, herein we developed 3D-printed structures from plant-based hydrogels for their inherent potential in biomedical applications. A series of 3D bio-hydrogels composed of aloe vera gel and TEMPO-oxidized cellulose nanofibrils were successfully printed through the direct ink writing method. Furthermore, the physical and structural features of the 3D-printed samples were evaluated to reveal they meet some preliminary requirements for the claimed applications. Although different research groups have proven the biocompatibility, non-toxicity, and cell compatibility of the AV and TOCNF hydrogels (Darpentigny et al., 2020; Huan et al., 2019; Rahman et al., 2017; Raj et al., 2020; Tehrani et al., 2016), further and more comprehensive evaluations, such as cytotoxicity assay and antibacterial test, are needed to specifically validate these 3D structures for biomedical applications.

4. Conclusion

In the current study, preparation, 3D printing, and characterization of bio-hydrogels composed of aloe vera/TEMPO-oxidized cellulose nanofibril (AV/TOCNF) were reported. The intrinsic shear-thinning behavior and excellent viscoelastic properties of AV and TOCNF hydrogels enabled successful 3D printing of the lattice structures employing the direct ink writing (DIW) technique. All inks were printed successfully with high precision and fidelity while avoiding issues such as swelling/shrinkage of the gel upon extrusion. The stability and mechanical performances of the samples improved through the addition of TOCNF due to the uniform dispersion of micro- and nano- nano-size fibrils into the AV gel. Furthermore, all samples illustrated high porosity (more than 80%) with high water uptake and retained capacity. The rheology data revealed a gel-like or solid-like behavior in which the elastic and loss moduli were independent of frequency. In addition, the results confirmed the higher values of G′ than G″, suggesting the interactions of quite strong hydrogen bonds with water and adjacent polysaccharide portions. Overall, the current study confirmed the possibility of DIW of AV/TOCNF bio-hydrogels to be printed with complex geometries, which might be interesting for the demanded biomedical applications.

CRediT authorship contribution statement

Hossein Baniasadi: Conceptualization, Methodology, Formal analysis, Investigation, Writing – original draft, Writing – review & editing, Visualization. **Rubina Ajdary:** Conceptualization, Methodology, Formal analysis, Investigation, Writing – original draft, Writing – review & editing, Visualization. **Jon Trifol:** Conceptualization, Methodology, Investigation, Writing – review & editing, Visualization. **Orlando J. Rojas:** Supervision, Funding acquisition, Writing – review & editing. **Jukka Seppälä:** Supervision, Funding acquisition, Writing – review & editing.

Acknowledgments

The authors would like to acknowledge funding support by the Academy of Finland's Biofuture 2025 program under project No. 2228357-4 (3D Manufacturing of Novel Biomaterials) and No. 327248 (ValueBiomat). This work made use of the facilities of Aalto University's Nanomicroscopy Center. The authors also would like to acknowledge the discussions with Dr. Janika Lehtonen and Dr. Arun Teotia.

Appendix A. Supplementary data

Supplementary data to this article can be found online at https://doi.org/10.1016/j.carbpol.2021.118114.

References

Abdel-Mohsen, A. M., Abdel-Rahman, R. M., Kubena, I., Kobera, L., Spotz, Z., Zboncak, M., … Jancar, J. (2020). Chitosan-glucan complex hollow fibers reinforced collagen wound dressing embedded with aloe vera. Part I: Preparation and characterization. *Carbohydrate Polymers, 230*, 115708.

Abdel-Mohsen, A. M., Frankova, J., Abdel-Rahman, R. M., Salem, A. A., Sahffie, N. M., Kubena, I., & Jancar, J. (2020). Chitosan-glucan complex hollow fibers reinforced collagen wound dressing embedded with aloe vera. II. Multifunctional properties to promote cutaneous wound healing. *International Journal of Pharmaceutics, 582* (September 2019), 119349. https://doi.org/10.1016/j.ijpharm.2020.119349

Abou-Yousef, H., Dacrory, S., Hasanin, M., Saber, E., & Kamel, S. (2021). Biocompatible hydrogel based on aldehyde-functionalized cellulose and chitosan for potential control drug release. *Sustainable Chemistry and Pharmacy, 21*, 100419.

Aghamohamadi, N., Sanjani, N. S., Majidi, R. F., & Nasrollahi, S. A. (2019). Preparation and characterization of Aloe vera acetate and electrospinning fibers as promising antibacterial properties materials. *Materials Science and Engineering: C, 94*, 445–452.

Ajdary, R., Ezazi, N. Z., Correia, A., Kemell, M., Huan, S., Ruskoaho, H. J., … Rojas, O. J. (2020). Multifunctional 3D-printed patches for long-term drug release therapies after myocardial infarction. *Advanced Functional Materials, 30*(34). https://doi.org/10.1002/adfm.202003440

Ajdary, R., Huan, S., Zanjanizadeh Ezazi, N., Xiang, W., Grande, R., Santos, H. A., & Rojas, O. J. (2019). Acetylated nanocellulose for single-component bioinks and cell proliferation on 3D-printed scaffolds. *Biomacromolecules, 20*(7), 2770–2778. https://doi.org/10.1021/acs.biomac.9b00527

Ajdary, R., Tardy, B. L., Mattos, B. D., Bai, L., & Rojas, O. J. (2020). Plant nanomaterials and inspiration from nature: Water interactions and hierarchically structured hydrogels. *Advanced Materials*, 2001085. https://doi.org/10.1002/adma.202001085

Al-Dulimi, Z., Wallis, M., Tan, D. K., Maniruzzaman, M., & Nokhodchi, A. (2020). 3D printing technology as innovative solutions for biomedical applications. *Drug Discovery Today, 26*(2), 360–383.

Alves, L., Ferraz, E., Lourenço, A. F., Ferreira, P. J., Rasteiro, M. G., & Gamelas, J. A. F. (2020). Tuning rheology and aggregation behaviour of TEMPO-oxidised cellulose nanofibrils aqueous suspensions by addition of different acids. *Carbohydrate Polymers*, 116109.

Angulo, D. E. L., Ambrosio, C. E., Lourenço, R., Gonçalves, N. J. N., Cury, F. S., & do Amaral Sobral, P. J.. (2019). Fabrication, characterization and in vitro cell study of gelatin-chitosan scaffolds: New perspectives of use of aloe vera and snail mucus for soft tissue engineering. *Materials Chemistry and Physics, 234*, 268–280.

Baniasadi, H., Ramazani, S. A., & A., & Mashayekhan, S.. (2015). Fabrication and characterization of conductive chitosan/gelatin-based scaffolds for nerve tissue engineering. *International Journal of Biological Macromolecules, 74*, 360–366. https://doi.org/10.1016/j.ijbiomac.2014.12.014

Bercea, M., Biliuta, G., Avadanei, M., Baron, R. I., Butnaru, M., & Coseri, S. (2019). Self-healing hydrogels of oxidized pullulan and poly (vinyl alcohol). *Carbohydrate Polymers, 206*, 210–219.

Bialik-Wąs, K., Pluta, K., Malina, D., Barczewski, M., Malarz, K., & Mrozek-Wilczkiewicz, A. (2020). Advanced SA/PVA-based hydrogel matrices with prolonged release of Aloe vera as promising wound dressings. *Materials Science and Engineering: C, August*, 111667. https://doi.org/10.1016/j.msec.2020.111667

Caló, E., & Khutoryanskiy, V. V. (2015). Biomedical applications of hydrogels: A review of patents and commercial products. *European Polymer Journal, 65*, 252–267.

Chao, F. C., Wu, M. H., Chen, L. C., Lin, H. L., Liu, D. Z., Ho, H. O., & Sheu, M. T. (2020). Preparation and characterization of chemically TEMPO-oxidized and mechanically disintegrated sacchachitin nanofibers (SCNF) for enhanced diabetic wound healing. *Carbohydrate Polymers, 229*(October 2019), 115507. https://doi.org/10.1016/j.carbpol.2019.115507

Coffigniez, M., Gremillard, L., Balvay, S., Lachambre, J., Adrien, J., & Boulnat, X. (2021). Direct-ink writing of strong and biocompatible titanium scaffolds with bimodal interconnected porosity. *Additive Manufacturing*, 101859.

Coseri, S., Biliuta, G., Zemljič, L. F., Srndovic, J. S., Larsson, P. T., Strnad, S., … Lindström, T. (2015). One-shot carboxylation of microcrystalline cellulose in the presence of nitroxyl radicals and sodium periodate. *RSC Advances, 5*(104), 85889–85897. https://doi.org/10.1039/c5ra16183e

Curti, F., Drăguşin, D.-M., Serafim, A., Iovu, H., & Stancu, I.-C. (2021). Development of thick paste-like inks based on superconcentrated gelatin/alginate for 3D printing of scaffolds with shape fidelity and stability. *Materials Science and Engineering: C, 122*, 111866.

Czaikoski, A., da Cunha, R. L., & Menegalli, F. C. (2020). Rheological behavior of cellulose nanofibers from cassava peel obtained by combination of chemical and physical processes. *Carbohydrate Polymers, 248*, 116744.

Dai, H., Zhang, H., Ma, L., Zhou, H., Yu, Y., Guo, T., Zhang, Y., & Huang, H. (2019). Green pH/magnetic sensitive hydrogels based on pineapple peel cellulose and polyvinyl alcohol: Synthesis, characterization and naringin prolonged release. *Carbohydrate Polymers, 209*, 51–61.

Darpentigny, C., Nonglaton, G., Bras, J., & Jean, B. (2020). Highly absorbent cellulose nanofibrils aerogels prepared by supercritical drying. *Carbohydrate Polymers, 229* (July 2019), 115560. https://doi.org/10.1016/j.carbpol.2019.115560

Das, P., Yuran, S., Yan, J., Lee, P. S., & Reches, M. (2015). Sticky tubes and magnetic hydrogels co-assembled by a short peptide and melanin-like nanoparticles. *Chemical Communications, 51*(25), 5432–5435. https://doi.org/10.1039/c4cc07671k

Demeter, M., Meltzer, V., Călina, I., Scărisoreanu, A., Micutz, M., & Kaya, M. G. A. (2020). Highly elastic superabsorbent collagen/PVP/PAA/PEO hydrogels cross-linked via e-beam radiation. *Radiation Physics and Chemistry*, 108898.

Dey, A., Bera, R., & Chakrabarty, D. (2015). Influence of Aloe vera on the properties of N-vinylpyrrolidone-acrylamide copolymer hydrogel. *Materials Chemistry and Physics, 168*, 168–179.

Du, H., Liu, W., Zhang, M., Si, C., Zhang, X., & Li, B. (2019). Cellulose nanocrystals and cellulose nanofibrils based hydrogels for biomedical applications. *Carbohydrate Polymers, 209*, 130–144.

Fan, J., Ifuku, S., Wang, M., Uetani, K., Liang, H., Yu, H., Song, Y., Li, X., Qi, J., & Zheng, Y. (2018). Robust nanofibrillated cellulose hydro/aerogels from benign solution/solvent exchange treatment. *ACS Sustainable Chemistry & Engineering, 6*(5), 6624–6634.

Fourmann, O., Hausmann, M. K., Neels, A., Schubert, M., Nyström, G., Zimmermann, T., & Siqueira, G. (2021). 3D printing of shape-morphing and antibacterial anisotropic nanocellulose hydrogels. *Carbohydrate Polymers, 117716*.

Ghorbani, M., Nezhad-Mokhtari, P., & Ramazani, S. (2020). Aloe vera-loaded nanofibrous scaffold based on Zein/Polycaprolactone/Collagen for wound healing. *International Journal of Biological Macromolecules, 153*, 921–930. https://doi.org/10.1016/j.ijbiomac.2020.03.036

Guo, X., & Mei, N. (2016). Aloe vera: A review of toxicity and adverse clinical effects. *Journal of Environmental Science and Health. Part C, 34*(2), 77–96.

Heinze, T. (2016). Cellulose chemistry and properties: Fibers, nanocelluloses and advanced materials. In *, 271. Advances in polymer science*. Springer. https://doi.org/10.1007/978-3-319-26015-0.

Hu, W., Wang, Z., Xiao, Y., Zhang, S., & Wang, J. (2019). Advances in crosslinking strategies of biomedical hydrogels. *Biomaterials Science, 7*(3), 843–855.

Hua, J., Liu, C., Ng, P. F., & Fei, B. (2021). Bacterial cellulose reinforced double-network hydrogels for shape memory strand. *Carbohydrate Polymers, 259*, 117737.

Huan, S., Mattos, B. D. B. D., Ajdary, R., Xiang, W., Bai, L., & Rojas, O. J. O. J. (2019). Two-phase emulgels for direct ink writing of skin-bearing architectures. *Advanced Functional Materials*, 1902990. https://doi.org/10.1002/adfm.201902990

Huang, S., Chen, H.-J., Deng, Y.-P., You, X., Fang, Q., & Lin, M. (2020). Preparation of novel stable microbicidal hydrogel films as potential wound dressing. *Polymer Degradation and Stability, 181*, 109349.

Jack, A. A., Nordli, H. R., Powell, L. C., Farnell, D. J. J., Pukstad, B., Rye, P. D., … Hill, K. E. (2019). Cellulose nanofibril formulations incorporating a low-molecular-weight alginate oligosaccharide modify bacterial biofilm development. *Biomacromolecules, 20*(8), 2953–2961. https://doi.org/10.1021/acs.biomac.9b00522

Jankowska, I., Pankiewicz, R., Pogorzelec-Glaser, K., Ławniczak, P., Łapiński, A., & Tritt-Goc, J. (2018). Comparison of structural, thermal and proton conductivity properties of micro-and nanocelluloses. *Carbohydrate Polymers, 200*, 536–542.

Jia, Y., Zheng, M., Xu, Q., & Zhong, C. (2019). Rheological behaviors of Pickering emulsions stabilized by TEMPO-oxidized bacterial cellulose. *Carbohydrate Polymers, 215*, 263–271.

Jiang, J., Oguzlu, H., & Jiang, F. (2021). 3D printing of lightweight, super-strong yet flexible all-cellulose structure. *Chemical Engineering Journal, 405*, 126668.

Jiang, Y., Zhou, J., Shi, H., Zhang, Q., Feng, C., & Xv, X. (2020). Preparation of cellulose nanocrystal/oxidized dextran/gelatin (CNC/OD/GEL) hydrogels and fabrication of a CNC/OD/GEL scaffold by 3D printing. *Journal of Materials Science, 55*(6), 2618–2635.

Kambe, Y., Mizoguchi, Y., Kuwahara, K., Nakaoki, T., Hirano, Y., & Yamaoka, T. (2020). Beta-sheet content significantly correlates with the biodegradation time of silk fibroin hydrogels showing a wide range of compressive modulus. *Polymer Degradation and Stability, 179*, 109240.

Khodabakhshi, D., Eskandarinia, A., Kefayat, A., Rafienia, M., Navid, S., Karbasi, S., & Moshtaghian, J. (2019). In vitro and in vivo performance of a propolis-coated polyurethane wound dressing with high porosity and antibacterial efficacy. *Colloids and Surfaces B: Biointerfaces, 178*, 177–184.

Kopač, T., Krajnc, M., & Ručigaj, A. (2020). A mathematical model for pH-responsive ionically crosslinked TEMPO nanocellulose hydrogel design in drug delivery systems. *International Journal of Biological Macromolecules, 168*, 695–707.

Li, J., Wu, C., Chu, P. K., & Gelinsky, M. (2020). 3D printing of hydrogels: Rational design strategies and emerging biomedical applications. *Materials Science & Engineering R: Reports, 140*(February), 100543. https://doi.org/10.1016/j.mser.2020.100543

Li, N., Chen, W., Chen, G., & Tian, J. (2017). Rapid shape memory TEMPO-oxidized cellulose nanofibers/polyacrylamide/gelatin hydrogels with enhanced mechanical strength. *Carbohydrate Polymers, 171*, 77–84.

Liu, W., Erol, O., & Gracias, D. H. (2020). 3D printing of an in situ grown MOF hydrogel with tunable mechanical properties. *ACS Applied Materials & Interfaces, 12*(29), 33267–33275.

Liu, Y., Wong, C.-W., Chang, S.-W., & Hsu, S. (n.d.). An injectable, self-healing phenol-functionalized chitosan hydrogel with fast gelling property and visible light-crosslinking capability for 3D printing. Acta Biomaterialia.

Łojewska, J., Miśkowiec, P., Łojewski, T., & Proniewicz, L. M. (2005). Cellulose oxidative and hydrolytic degradation: In situ FTIR approach. *Polymer Degradation and Stability, 88*(3), 512–520. https://doi.org/10.1016/j.polymdegradstab. 2004.12.012

Lu, J., Han, X., Dai, L., Li, C., Wang, J., Zhong, Y., Yu, F., & Si, C. (2020). Conductive cellulose nanofibrils-reinforced hydrogels with synergetic strength, toughness, self-adhesion, flexibility and adjustable strain responsiveness. *Carbohydrate Polymers, 250*, 117010.

Lu, P., Liu, R., Liu, X., & Wu, M. (2018). Preparation of self-supporting bagasse cellulose nanofibrils hydrogels induced by zinc ions. *Nanomaterials, 8*(10), 800.

Lu, P., Yang, Y., Liu, R., Liu, X., Ma, J., Wu, M., & Wang, S. (2020). Preparation of sugarcane bagasse nanocellulose hydrogel as a colourimetric freshness indicator for intelligent food packaging. *Carbohydrate Polymers, 249*, 116831.

Luo, B., Chen, H., Zhu, Z., Xie, B., Bian, C., & Wang, Y. (2018). Printing single-walled carbon nanotube/Nafion composites by direct writing techniques. *Materials & Design, 155*, 125–133.

Ma, C., Wang, Y., Jiang, Z., Cao, Z., Yu, H., Huang, G., Wu, Q., Ling, F., Zhuang, Z., & Wang, H. (2020). Wide-range linear viscoelastic hydrogels with high mechanical properties and their applications in quantifiable stress-strain sensors. *Chemical Engineering Journal, 125697*.

Ma, T., Lv, L., Ouyang, C., Hu, X., Liao, X., Song, Y., & Hu, X. (2021). Rheological behavior and particle alignment of cellulose nanocrystal and its composite hydrogels during 3D printing. *Carbohydrate Polymers, 253*, 117217.

Moud, A. A., Kamkar, M., Sanati-Nezhad, A., Hejazi, S. H., & Sundararaj, U. (2021). Viscoelastic properties of poly (vinyl alcohol) hydrogels with cellulose nanocrystals fabricated through sodium chloride addition: Rheological evidence of double network formation. *Colloids and Surfaces A: Physicochemical and Engineering Aspects, 609*(September 2020), 125577. https://doi.org/10.1016/j.colsurfa.2020.125577

Nazarnezhada, S., Abbaszadeh-Goudarzi, G., Samadian, H., Khaksari, M., Ghatar, J. M., Khastar, H., … Salehi, M. (2020). Alginate hydrogel containing hydrogen sulfide as the functional wound dressing material: In vitro and in vivo study. *International Journal of Biological Macromolecules, 164*, 3323–3331.

Onkarappa, H. S., Prakash, G. K., Pujar, G. H., Kumar, C. R. R., Latha, M. S., & Betageri, V. S. (2020). Hevea brasiliensis mediated synthesis of nanocellulose: Effect of preparation methods on morphology and properties. *International Journal of Biological Macromolecules, 160*, 1021–1028.

Patruni, K., Chakraborty, S., & Pavuluri, S. R. (2018). Rheological, functional and morphological characterization of reconstituted Aloe vera gels at different levels of pH and concentration: Novel concepts of reconstituted Aloe vera gels formation. *International Journal of Biological Macromolecules, 120*, 414–421.

Pillai, M. M., Tran, H. N., Sathishkumar, G., Manimekalai, K., Yoon, J. H., Lim, D. Y., … Bhattacharyya, A. (2021). Symbiotic culture of nanocellulose pellicle: A potential matrix for 3D bioprinting. *Materials Science and Engineering C, 119*(September 2020), 111552. https://doi.org/10.1016/j.msec.2020.111552

Rahman, S., Carter, P., & Bhattarai, N. (2017). Aloe vera for tissue engineering applications. *Journal of Functional Biomaterials, 8*(1), 6.

Raj, R. M., Duraisamy, N., & Raj, V. (2020). Drug loaded chitosan/aloe vera nanocomposite on Ti for orthopedic applications. *Materials Today: Proceedings*. https://doi.org/10.1016/j.matpr.2020.10.772

Santmarti, A., Tammelin, T., & Lee, K. Y. (2020). Prevention of interfibril hornification by replacing water in nanocellulose gel with low molecular weight liquid poly

(ethylene glycol). *Carbohydrate Polymers, 250*(August), 116870. https://doi.org/10.1016/j.carbpol.2020.116870

Seo, J. W., Shin, S. R., Lee, M.-Y., Cha, J. M., Min, K. H., Lee, S. C., … Bae, H. (2020). Injectable hydrogel derived from chitosan with tunable mechanical properties via hybrid-crosslinking system. *Carbohydrate Polymers, 251*, 117036.

Shahini, A., Yazdimamaghani, M., Walker, K. J., Eastman, M. A., Hatami-Marbini, H., Smith, B. J., … Tayebi, L. (2013). 3D conductive nanocomposite scaffold for bone tissue engineering. *International Journal of Nanomedicine, 9*(1), 167–181. https://doi.org/10.2147/IJN.S54668

Shefa, A. A., Sultana, T., Park, M. K., Lee, S. Y., Gwon, J. G., & Lee, B. T. (2020). Curcumin incorporation into an oxidized cellulose nanofiber-polyvinyl alcohol hydrogel system promotes wound healing. *Materials and Design, 186*, 108313. https://doi.org/10.1016/j.matdes.2019.108313

Silva, K. M. M. N., de Carvalho, D.É. L., Valente, V. M. M., Rubio, J. C. C., Faria, P. E., & Silva-Caldeira, P. P. (2019). Concomitant and controlled release of furazolidone and bismuth (III) incorporated in a cross-linked sodium alginate-carboxymethyl cellulose hydrogel. *International Journal of Biological Macromolecules, 126*, 359–366.

Siqueira, G., Kokkinis, D., Libanori, R., Hausmann, M. K., Gladman, A. S., Neels, A., … Studart, A. R. (2017). Cellulose nanocrystal inks for 3D printing of textured cellular architectures. *Advanced Functional Materials, 27*(12). https://doi.org/10.1002/adfm.201604619

Smith, P. T., Basu, A., Saha, A., & Nelson, A. (2018). Chemical modification and printability of shear-thinning hydrogel inks for direct-write 3D printing. *Polymer, 152*, 42–50.

Su, C., Liu, J., Yang, Z., Jiang, L., Liu, X., & Shao, W. (2020). UV-mediated synthesis of carboxymethyl cellulose/poly-N-isopropylacrylamide composite hydrogels with triple stimuli-responsive swelling performances. *International Journal of Biological Macromolecules, 161*, 1140–1148.

Tehrani, Z., Nordli, H. R., Pukstad, B., Gethin, D. T., & Chinga-Carrasco, G. (2016). Translucent and ductile nanocellulose-PEG bionanocomposites—A novel substrate with potential to be functionalized by printing for wound dressing applications. *Industrial Crops and Products, 93*, 193–202. https://doi.org/10.1016/j.indcrop.2016.02.024

Thomas, D., Nath, M. S., Mathew, N., R, R., Philip, E., & Latha, M. S. (2020). Alginate film modified with aloevera gel and cellulose nanocrystals for wound dressing application: Preparation, characterization and in vitro evaluation. *Journal of Drug Delivery Science and Technology, 59*(March), 101894. https://doi.org/10.1016/j.jddst.2020.101894

Trifol, J., Marin Quintero, D. C., & Moriana, R. (2021). Pine cone biorefinery: integral valorization of residual biomass into lignocellulose nanofibrils (LCNF)-reinforced composites for packaging. *ACS Sustainable Chemistry & Engineering, 9*(5), 2180–2190.

Wahid, F., Zhao, X.-J., Jia, S.-R., Bai, H., & Zhong, C. (2020). Nanocomposite hydrogels as multifunctional systems for biomedical applications: Current state and perspectives. *Composites Part B: Engineering*, 108208.

Wang, J., Liu, Y., Zhang, X., Rahman, S. E., Su, S., Wei, J., … Sennoune, S. R. (2021). 3D printed agar/calcium alginate hydrogels with high shape fidelity and tailorable mechanical properties. *Polymer, 214*, 123238.

Wang, Q., Pan, X., Guo, J., Huang, L., Chen, L., Ma, X., Cao, S., & Ni, Y. (2021). Lignin and cellulose derivatives-induced hydrogel with asymmetrical adhesion, strength, and electriferous properties for wearable bioelectrodes and self-powered sensors. *Chemical Engineering Journal, 414*, 128903.

Wei, J., Wang, B., Li, Z., Wu, Z., Zhang, M., Sheng, N., … Chen, S. (2020). A 3D-printable TEMPO-oxidized bacterial cellulose/alginate hydrogel with enhanced stability via nanoclay incorporation. *Carbohydrate Polymers, 238*, 116207.

Wei, J., Chen, Y., Liu, H., Du, C., Yu, H., Ru, J., & Zhou, Z. (2016). Effect of surface charge content in the TEMPO-oxidized cellulose nanofibers on morphologies and properties of poly(N-isopropylacrylamide)-based composite hydrogels. *Industrial Crops and Products, 92*, 227–235. https://doi.org/10.1016/j.indcrop.2016.08.006

Xue, H., Hu, L., Xiong, Y., Zhu, X., Wei, C., Cao, F., Zhou, W., Sun, Y., Endo, Y., & Liu, M. (2019). Quaternized chitosan-Matrigel-polyacrylamide hydrogels as wound dressing for wound repair and regeneration. *Carbohydrate Polymers, 226*, 115302.

Yang, J., An, X., Liu, L., Tang, S., Cao, H., Xu, Q., & Liu, H. (2020). Cellulose, hemicellulose, lignin, and their derivatives as multi-components of bio-based feedstocks for 3D printing. *Carbohydrate Polymers*, 116881.

Yang, Y., Lu, Y. T., Zeng, K., Heinze, T., Groth, T., & Zhang, K. (2020). Recent progress on cellulose-based ionic compounds for biomaterials. *Advanced Materials*, 2000717. https://doi.org/10.1002/adma.202000717

Ye, J., Fu, S., Zhou, S., Li, M., Li, K., Sun, W., & Zhai, Y. (2020). Advances in hydrogels based on dynamic covalent bonding and prospects for its biomedical application. *European Polymer Journal*, 110024.

Yin, J., & Xu, L. (2020). Batch preparation of electrospun polycaprolactone/chitosan/aloe vera blended nanofiber membranes for novel wound dressing. *International Journal of Biological Macromolecules, 160*, 352–363. https://doi.org/10.1016/j.ijbiomac.2020.05.211

Yue, Y., Gu, J., Han, J., Wu, Q., & Jiang, J. (2021). Effects of cellulose/salicylaldehyde thiosemicarbazone complexes on PVA based hydrogels: Portable, reusable, and high-precision luminescence sensing of Cu2+. *Journal of Hazardous Materials, 401*, 123798.

Zhang, X., Pan, Y., Li, S., Xing, L., Du, S., Yuan, G., Li, J., Zhou, T., Xiong, D., & Tan, H. (2020). Doubly crosslinked biodegradable hydrogels based on gellan gum and chitosan for drug delivery and wound dressing. *International Journal of Biological Macromolecules, 164*, 2204–2214.

Zhang, Y., Mao, J., Xu, T., Zhang, Z., Yang, B., Mao, J., & Yang, X. (2019). Preparation of a novel fracturing fluid with good heat and shear resistance. *RSC Advances, 9*(3), 1199–1207. https://doi.org/10.1039/C8RA09483G